DEFINITION OF DISTURBANCE REJECTION REQUIREMENTS FOR IMPROVED VIBRATIONAL RIDE COMFORT

Tim Burkhardt
Research Associate

Süleyman Özkurt
Research Associate
University of Stuttgart
Stuttgart, Germany

Walter Fichter
Professor

ABSTRACT

In manned aviation, the improvement of the ride comfort becomes increasingly important. The phenomena that cause discomfort during flight are divided into two types. The first is the whole-body vibration mainly introduced through the high-frequency rotation of the rotor. The second type of discomfort is kinetosis. Passengers who experience kinetosis can suffer from disorientation, nausea and vomiting. It is initiated by low-frequency oscillations below 0.5 Hz. These are mainly caused by the reaction to disturbances from the pilot or the automatic flight control system. The severity of kinetosis can be mitigated with a proper controller design. However, no metric exists to take the kinetosis effect into account at the controller design. Nevertheless, there are already models to describe the development of kinetosis depending on the flight maneuvers. These models are either too simplified to depict the complex processes or are nonlinear and therefore cannot be taken into account in linear control. One of these nonlinear models is already adapted to the helicopter environment. It predicts the intensity of kinetosis depending on occurring translational and rotational movements. This paper describes the systematic analysis of this model resulting in new disturbance rejection bandwidths of the flight control system that ensure a reduction of kinetosis. The model is linearized and its characteristics are analyzed and compared to the nonlinear model. Based on the transfer functions of the linearized model, new requirements for the disturbance rejection bandwidths are identified. These requirements are stricter and can therefore serve as an extension of the ADS-33 requirements. Controllers that are designed to meet the new disturbance rejection bandwidths result in a kinetosis reduction of more than 20 % compared to controllers that comply with the bandwidths of ADS-33. This shows that the new requirements result in a significant reduction of kinetosis enabling a smooth ride in passenger transport.

INTRODUCTION

As illustrated in Ref. 1, automatic flight control systems (AFCSs) in rotorcraft are typically designed according to handling qualities and stability requirements such as those from Refs. 2, 3. From a pilot's point of view, the compliance of these requirements leads to good flight characteristics of rotorcraft. However, the passengers' impression of the flight characteristics, i.e., ride comfort, is not addressed by these requirements, although their importance will dominate in future automated, unpiloted rotorcraft. Consequently, ride comfort will become a decisive sales argument in the future. The phenomena that trigger vibrational discomfort in rotorcraft are kinetosis and whole-body vibrations. Both phenomena have different causes and must be treated accordingly. The proposed paper focuses on kinetosis since whole-body vibrations are currently well-handled by the rotorcraft industry. Kinetosis, known as motion sickness (MS), is considered a medical condition with accompanying symptoms such as vomiting, sweating, headaches, and nausea. According to Griffin (Ref. 4, ch. 7), kinetosis is provoked by low-frequency motion which occurs over longer periods. As shown in Refs. 5, 6, kinetosis in rotorcraft is caused by AFCS counterreactions to turbulences. Further, according to the results in Ref. 6, the severity of kinetosis depends on the control parameters and the underlying disturbance rejection properties of the closed-loop. Nevertheless, the disturbance rejection requirements defined in Ref. 2 are boundary conditions for the design of AFCS, but they are not designed for flights under turbulent conditions. Also, they only take into account the flight characteristics from a pilots point of view, ignoring the passengers' impressions. Therefore, it has to be checked if these requirements are appropriate to mitigate kinetosis. In this paper, this is performed by the design of an attitude command attitude hold architecture (ACAH) that fulfills these requirements. This baseline closed-loop system is exposed to long-term turbulences within a simulation framework to calculate the kinetosis severity from the rigid-body states of the rotorcraft.

Since current requirements for flight controllers are not sufficient to suppress kinetosis in turbulence, existing requirements must be modified for kinetosis. For the derivation of new requirements, it is required to understand the transfer behavior of rotorcraft states onto the kinetosis of the passengers. Hence, the existing nonlinear kinetosis model from Ref. 6 is linearized around a trim point of the helicopter. This linearization provides a transfer matrix that describes the input-output behavior from measurable rotorcraft states to the subjective vertical conflict vector which indicates the severity of kinetosis. Based on this transfer matrix, new disturbance rejection bandwidths (DRBs) are derived from the peak frequency and a controller is designed to comply with these DRBs. Using these requirements for the controller design, the kinetosis severity of the new closed-loop system is calculated within a simulation framework and compared to the initial design. Hence, the contributions of this paper are:

- Linearization of a kinetosis model and analysis of the characteristics causing kinetosis.
- Derivation of new requirements for kinetosis suppression.
- Comparison of the kinetosis serverity between the different designs, demonstrating a significant reduction in passenger kinetosis.

First, the existing approaches for modeling kinetosis are presented. Second, the linearized model is calculated and the differences to the nonlinear model as well as the characteristics of the linear model are worked out. In the next step, the initial and the modified controller design are presented. Finally, the results of the controller simulations are presented and conclusions are drawn.

KINETOSIS MODELS

In the field of maritime navigation, where vertical motion is primarily responsible for inducing motion sickness, models have already been developed for the prediction of kinetosis. These models can be expanded to describe a helicopter environment in terms of six degrees of freedom. An established model is proposed by Griffin (Ref. 4) in ISO2631-1 (Ref. 7). In this calculation procedure, only the vertical acceleration a_z is measured. In order to weight frequencies with a high sensitivity to kinetosis, the measured acceleration a_z is filtered with a weighing function to $a_{z,w}$. This weighted acceleration is reduced to the scalar motion sickness dose value MSDV_z using Eq. (1)

$$\mathrm{MSDV}_z = \sqrt{\int_0^T a_{z,w}^2(t)dt}, \tag{1}$$

where T is the time the subject is exposed to the vibration. This MSDV_z is proportional to the vomiting incidence VI. This is the percentage of people vomiting while being exposed to the vibration. The relationship is shown in Eq. (2)

$$\mathrm{VI} = \frac{1}{3}\mathrm{MSDV}_z. \tag{2}$$

In further studies, Griffin examined the impact of lateral vibrations on kinetosis showing that this model can be expanded to all spatial directions. The calculation structure only integrates the acceleration over time. As a result, MSDV_z and VI can only increase over time. This may be accurate for a naval environment with constant vibrations. However, it cannot depict the complex helicopter environment. Here, the appearance of turbulences must be modeled by more complex dynamics also allowing the kinetosis to decrease.

A system-driven approach is the subjective vertical mismatch model (Ref. 8) based on the subjective vertical conflict theory which states that kinetosis is provoked by a mismatch of the measured subjective vertical (i.e., gravity vector) of the vestibular system and an estimated subjective vertical of the human neural memory. The model is also one dimensional with the vertical acceleration as input. According to (Ref. 9), the acceleration is low-pass filtered to estimate the subjective vertical out of the gravitational acceleration. As shown in Figure 1, the estimated subjective vertical $\hat{v}$ is calculated using an observer model. The conflict c between the model and the

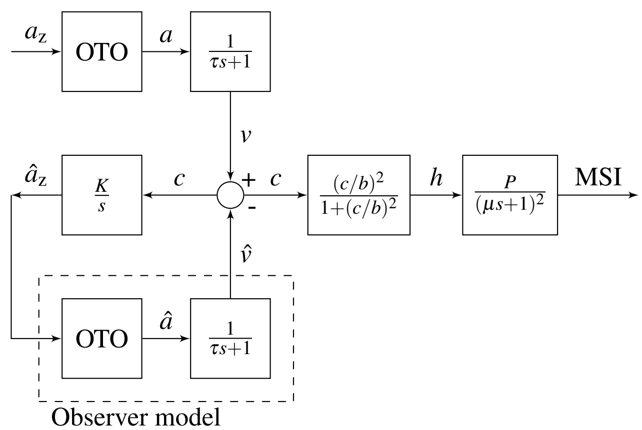

Figure 1: Scheme of the subjective vertical mismatch model from Ref. 8.

observer is then proceeded with a second order hill function. This normalizes the conflict to a value between 0 and 1. Afterwards, the result gets delayed using a second order low-pass filter. This allows the discomfort to increase and decrease in a longer time. The result is then rescaled using $P = 80$ to get the motion sickness incidence MSI, also a metric that shows the percentage of people vomiting because of the vibration.

Extension to Six Degrees of Freedom

The subjective vertical mismatch model from Ref. 8 is based on studies only in the vertical direction and calculates the motion sickness only using the vertical acceleration. In Ref. 10, this model is extended to six degrees of freedom as shown

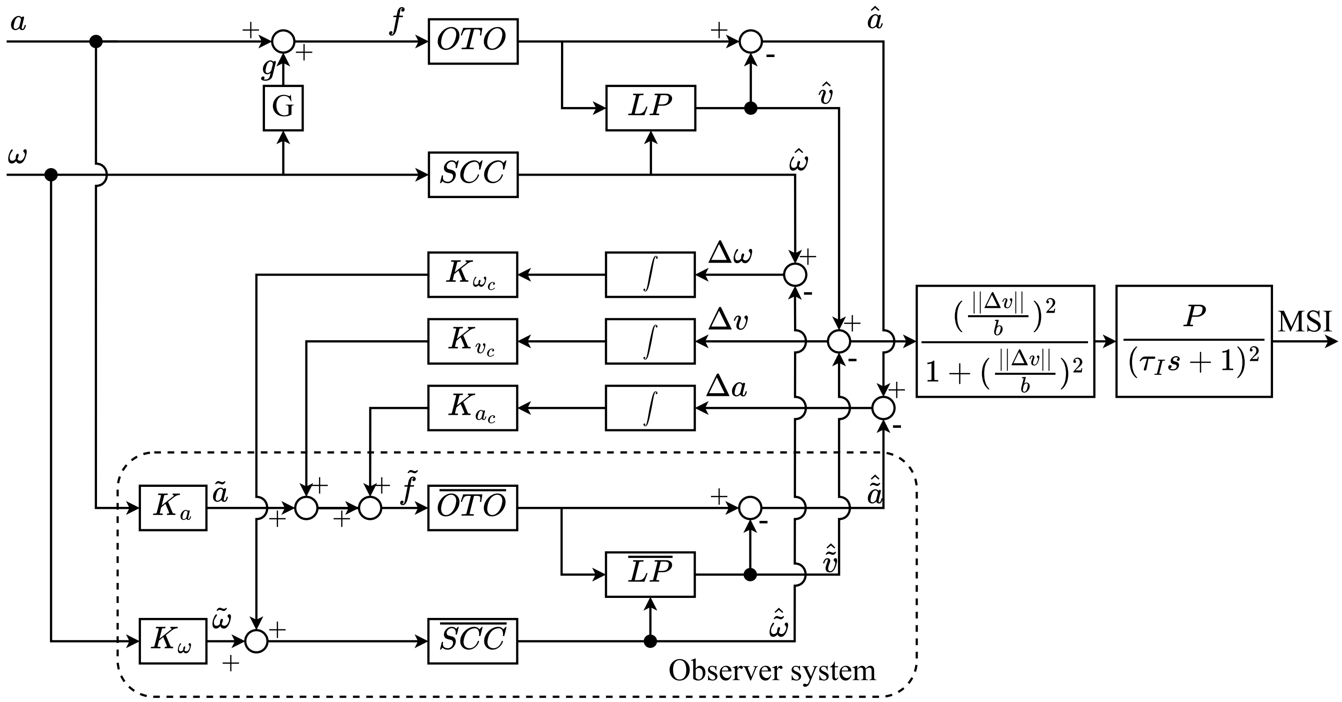

Figure 2: Extended subjective vertical mismatch model, (Ref. 10).

in Figure 2. Here, a coordinate system is defined, the head-related reference system. In the upright sitting position, it is assumed that the system is parallel to the body fixed system of the rotorcraft with differently defined direction of the axes. In the following, all vectors of the nonlinear kinetosis system are used in the head-related reference system. The calculation procedure is based on the subjective vertical mismatch model (Ref. 8). The acceleration a and the rotational speed ω are the input vectors. For the model, but not for the observer system, the additional acceleration g is added to the translational acceleration a. The differential equation of this gravitational acceleration resulting from the rotational speed is given in Eq. (3). The G-block thus describes the temporal change in gravity due to rotational motion

$$\frac{dg}{dt} = -\omega \times g. \tag{3}$$

The LP-block is used to estimate the own subjective vertical position vector. It now includes the rotational within the estimation of the subjective position. This is realized by the differential Eq. (4)

$$\frac{dv}{dt} = \frac{1}{\tau}(f - v) - \omega \times v. \tag{4}$$

The transfer function of the semicircular canals (SCC) is described by Eq. (5). τ_d is the dominant time constant and τ_a is the adaptive time constant. For the internal estimation of the SCC transfer function in the observer model, the adaptive time constant τ_a is neglected, as shown in Eq. (6), (Ref. 11)

$$\hat{\omega}_i = \frac{\tau_d \tau_a s^2}{(\tau_d s + 1)(\tau_a s + 1)} \omega_i \qquad (i = x, y, z), \tag{5}$$

$$\hat{\hat{\omega}}_i = \frac{\tau_d s}{\tau_d s + 1} \tilde{\omega}_i \qquad (i = x, y, z). \tag{6}$$

In the inertial observer model (dashed box in Figure 2), the factor K_a is included for estimating the accuracy of the translational acceleration and the factor K_ω for estimating the accuracy of the angular velocity. With a value of 1, the estimate by the human would be perfect, with 0 the prediction would be completely missing. The empirically determined factors K_{a_c}, K_{ω_c} and K_{v_c} scale the influence of the deviations. The deviations Δa, $\Delta\omega$ and Δv are the difference between the actual states and the states estimated by the observer system. Before the deviations are fed back into the observer system, they are integrated, which influences the learning process. The deviation between the actual and estimated subjective vertical Δv is also included as an error in the calculation of MSI. With the standard of Δv as input, the calculation of MSI is analogous to that of the one-dimensional dynamic model. A detailed description of the calculation process can be found in Ref. 10. The extension to six degrees of freedom are not validated in studies and the used parameters are only assumptions, calculated with generic sinusoidal oscillations in vertical direction. Therefore, in a former study (Ref. 6), the structure and parameters of this model were modified to fit to real helicopter data. Here, all degrees of freedom were taken into account for the estimation of the parameters. Additionally, the output scale was changed to the fast motion sickness scale (FMSS), a scale from 0 to 20 indicating the amount of motion sickness a person experiences. In the following, the modified model and parameter values from Ref. 6 are used.

LINEARIZED KINETOSIS MODEL

For the derivation of new disturbance rejection requirements, a linear kinetosis model is required. From Ref. 6, the nonlinear differential Eq. (13) in the Appendix is derived. The structure of the nonlinear differential equation f and output equation h are shown in Eq. (7)

$$\begin{aligned}\dot{\vec{x}}_{\mathrm{MS}} &= f(\vec{x}_{\mathrm{MS}}, {}_E\vec{u}_{\mathrm{MS}}) \\ \Delta\dot{\vec{v}} &= h(\vec{x}_{\mathrm{MS}}, {}_E\vec{u}_{\mathrm{MS}}),\end{aligned} \tag{7}$$

where $\vec{x}_{\mathrm{MS}}$ represents motion sickness states, ${}_E\vec{u}_{\mathrm{MS}} = [{}_E\vec{a}, {}_E\vec{g}, {}_E\vec{\omega}]^T$ is the input vector consisting of specific forces, euler angles and angular rates of the rotorcraft in the head reference frame ${}_E$. $\Delta\dot{\vec{v}}$ represents the subjective vertical conflict vector. $\Delta\dot{\vec{v}}$ is the output of the system since it correlates to the FMSS. The nonlinear system of equations schematized in Eq. (7) is given in Eq. (13) in the Appendix.
The nonlinear system in Eq. (7) is transformed into a linear state space model of the form $\dot{\vec{x}}_{\mathrm{MS}} = A_{\mathrm{MS}}\vec{x}_{\mathrm{MS}} + B_{\mathrm{MS}}\vec{u}_{\mathrm{MS}}$. It is linearized around a steady flight state with $\vec{x}_{\mathrm{MS},0} = 0$ and ${}_E\vec{u}_{\mathrm{MS},0} = 0$. Here, the accelerations, angles and angular rates are zero at the considered steady flight state.
The control inputs ${}_E\vec{u}_{\mathrm{MS}} = [{}_E\vec{a}, {}_E\vec{g}, {}_E\vec{\omega}]^T$ in this system represent the translational accelerations, the accelerations due to the gravity vector and the angular rates. These are converted from the head reference frame ${}_E$ to the body fixed system ${}_f$ by reversing the direction of the y- and z-axis. The input of the gravitational vector ${}_f g$ is transformed that it is described by the Euler angles $\vec{\varphi}$. Therefore, the approximation by ${}_f\vec{g} = {}_g\vec{g}_\times \Delta\vec{\varphi}$ is used where ${}_g\vec{g}_\times$ is the matrix notation of the cross product of ${}_g\vec{g}$. Consequently, all control inputs for this system $\vec{u}_{\mathrm{MS}} = [{}_f\vec{a}, {}_f\vec{g}, {}_f\vec{\omega}]^T$ can be directly derived from the state variables of the helicopter. The linearized system is described in Eq. (14). The input is described in Eq. (15), with the 7 state vectors shown divided into their x, y and z components.

Comparison Between Nonlinear and Linear Model

Due to the linearization of Eq. (13) to Eq. (14) and Eq. (15), the linear and the nonlinear prediction model differ. Since most terms are linear, these differences between the models come from the mixed terms of the nonlinear model. This influences the equations for the parameters $\dot{\vec{v}}_s$ and $\dot{\hat{\vec{v}}}_s$ in which mixed terms with cross products exist. Since the linearization is performed at a steady flight state with $\vec{x}_{\mathrm{MS},0} = 0$ and $\vec{u}_{\mathrm{MS},0} = 0$, these terms are neglected in the linear model. As a result, the rows 3 to 5 of the system in Eq. (13) as well as the input of the rotational speed ${}_f\omega$ are decoupled from the rest of the system. The reduced linear representation is shown in Eq. (8) and Eq. (9)

$$A_{\mathrm{red}}\vec{x}_{\mathrm{red}} = \begin{bmatrix} -\frac{1}{\tau} & 0 & 0 & 0 \\ 0 & -\frac{1}{\tau} & \frac{1}{\tau}K_{ac} & \frac{1}{\tau}K_{vc} \\ -1 & 1 & -K_{ac} & -K_{vc} \\ 1 & -1 & 0 & 0 \end{bmatrix} \begin{bmatrix} v_s \\ \hat{v}_s \\ \Delta a_I \\ \Delta v_I \end{bmatrix}, \tag{8}$$

$$B_{\mathrm{red}}\vec{u}_{\mathrm{red}} = \begin{bmatrix} \frac{1}{\tau_x} & 0 & 0 & 0 & -g\frac{1}{\tau_x} \\ 0 & -\frac{1}{\tau_y} & 0 & -g\frac{1}{\tau_y} & 0 \\ 0 & 0 & -\frac{1}{\tau_z} & 0 & 0 \\ \frac{1}{\tau_x}K_a & 0 & 0 & 0 & 0 \\ 0 & -\frac{1}{\tau_y}K_a & 0 & 0 & 0 \\ 0 & 0 & -\frac{1}{\tau_z}K_a & 0 & 0 \\ -K_a+1 & 0 & 0 & 0 & -g \\ 0 & K_a-1 & 0 & -g & 0 \\ 0 & 0 & K_a-1 & 0 & 0 \\ 0 & 0 & 0 & 0 & 0 \\ 0 & 0 & 0 & 0 & 0 \\ 0 & 0 & 0 & 0 & 0 \end{bmatrix} \begin{bmatrix} {}_f a_x \\ {}_f a_y \\ {}_f a_z \\ \Delta\phi \\ \Delta\theta \end{bmatrix}. \tag{9}$$

The influence of these simplifications on the tranlsational and rotational movement is analyzed in the following. For translational movements, without the occurrence of rotations, the calculations of both models are identical. This can be verified by setting the external inputs for ${}_k\vec{\omega}$ in Eq. (13) to zero. This results in $\vec{\omega}_{s2}$, $\dot{\vec{\omega}}_{s2}$ and $\ddot{\vec{\omega}}_{s2}$ being zero as well as $\hat{\vec{\omega}}_{s1}$ and $\dot{\hat{\vec{\omega}}}_{s1}$. The resulting system only consists of linear terms that all appear in Eq. (14) and Eq. (15) and therefore, all calculation steps are identical for translational accelerations.
As already stated, lines 3 to 5 are decoupled from the system through the linearization as well as the angular velocity ${}_f\omega$. Therefore, this input also does not influence the value of the kinetosis. Instead, the discomfort through rotational movement is only created through the change of the direction of gravity. With simulations, it can be shown that this is the driving parameter for the kinetosis. In Figure 3 the linearized and the nonlinear model were used to simulate kinetosis as a result of sine inputs. Only rotational pitch inputs were given

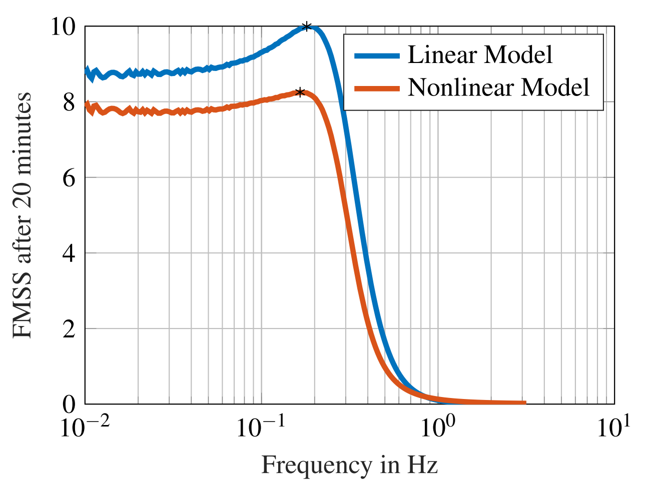

Figure 3: FMSS score for different frequencies with both models in pitch direction.

with an amplitude of ${}_{f}\omega_y = 0.2/s$. The final kinetosis value after 20 minutes of exposure time were taken for frequencies between 0.01 and 3 Hz. The simulation was also performed with different amplitudes showing similar or smaller differences. It can be seen that shape of the curves are not changed qualitatively. The value of the kinetosis is higher within the linearized model and the peak frequency of the kinetosis has increased from 0.165 Hz to 0.18 Hz. However, the shape does not change significantly. This shows that the main influence of rotational discomfort is given through the change of the gravitational direction, and therefore, the model can be used for the prediction and mitigation of kinetosis.

Derivation of the Transfer Function

Based on the linearized model, the transfer matrix, schematized in Eq. (10) is derived. The full matrix is given in Eq. (16) in the Appendix. It describes the transfer from the input $\vec{u}_{\mathrm{MS}}$ to the conflict $\Delta\vec{v}$

$$G_{\mathrm{MS}} = \begin{bmatrix} {}_{\Delta vx}G_{fa_x} & {}_{\Delta vx}G_{fa_y} & \cdots & {}_{\Delta vx}G_r \\ {}_{\Delta vy}G_{fa_x} & {}_{\Delta vy}G_{fa_y} & \cdots & {}_{\Delta vy}G_r \\ {}_{\Delta vz}G_{fa_x} & {}_{\Delta vz}G_{fa_y} & \cdots & {}_{\Delta vz}G_r \end{bmatrix}. \tag{10}$$

It can be seen that the angular velocity has no influence on the discomfort due to the approximation. Also the attitude angles only have influence in specific directions. Here, the pitch angle θ contributes only to the subjective vertical conflict in the longitudinal direction while the roll angle ϕ contributes to the subjective vertical conflict in the lateral direction. The yaw angle does not contribute to the vertical conflict. Consequently, couplings do not exist. Figure 4 shows the bode plots of the longitudinal acceleration and the pitch angle to the conflict in x-direction. The peak of the discomfort caused by a longitudinal acceleration ${}_{\Delta vx}G_{fa_x}$ is at 0.27 Hz, the one of the pitch angle ${}_{\Delta vx}G_{fa_\theta}$ at 0.23 Hz. In general the peak frequencies of all inputs for one conflict direction are located close to each other. The influence of the translational acceleration in each direction is small compared to the influence of the angles. The same appears for the y-direction with an input of lateral acceleration and the roll angle as shown in Figure 10. Therefore, roll and pitch angles are detected as the main contributors to the subjective vertical conflict. It is therefore possible to reduce the effect of kinetosis by avoiding these frequencies. This can be achieved through additional requirements in the controller design. Since an ACAH control architecture is considered, this allows the focus on the transfer functions ${}_{\Delta vx}G_\theta$ and ${}_{\Delta vy}G_\phi$ for the derivation of new disturbance rejection requirements.

INITIAL CONTROLLER DESIGN

An ACAH control architecture given in Figure 5 is considered since the rotorcraft model is trimmed at low speed.
The output $\vec{y} = [u, v, w, p, q, r, \phi, \theta, \psi]^T$ of the coupled rotorcraft model $G(s)$ as well as the decoupled system G_{dec} contains the rigid-body states. They serve as input to the kinetosis model from Ref. 6. The kinetosis model provides the

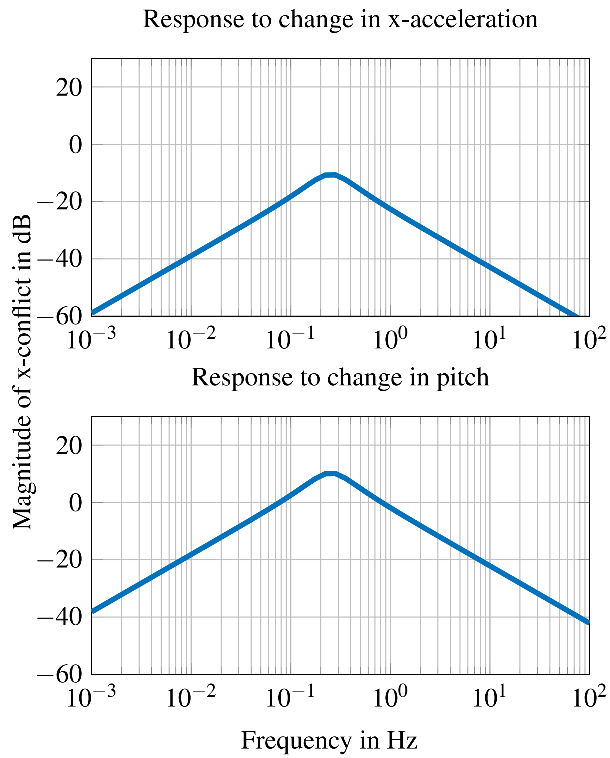

Figure 4: System response of the conflict to exemplary inputs.

FMSS, which ranges from 0 to 20, as an indicator of the sickness severity. The input $\vec{r} = [w, \phi, \theta, \psi]^T_{\mathrm{cmd}}$ contains the commanded states. The matrix C_{fb} reduces the output to the states to be tracked. The control input $\vec{u} = [d\theta, d\alpha, d\beta, d\delta]^T$ consists of percentage values of the controls in the collective, lateral, longitudinal, and yaw axis. The controller K is determined for a nominal design model $G_{\mathrm{dec}}(s)$. The nominal design model is determined from $G(s)$ by assuming quasi-static rotor behavior and performing decoupling with the feedforward and feedback matrices M_d and K_d. The matrices are calculated according to the decoupling procedure of Falb and Wolowich (Ref. 12). The approach is also stabilizing the rotorcraft through the choice of appropriate matrices. The decoupling allows to establish single-input single-output (SISO) controller for tracking in the corresponding control axis. Hence, the controller K is only used for tracking the commanded states. Further, the controller K is realized as a proportional-integral (PI) controller for each control axes. The integral and proportional gains of each control channel are determined balancing between robustness and performance specifications according to Refs. 13, 14. The gains are tuned such that the phase margin of the open-loop system is approximately 60° and the specified disturbance rejection bandwidths (DRBs) defined in ADS-33 (Ref. 2) are achieved for the sensitivity functions. The DRB is defined as frequency where the sensitivity function first reaches -3 dB. The control equivalent turbulence input (CETI) model from Ref. 15 is used to expose the rotorcraft to turbulences. Since the CETI model is derived for a coupled system, its output is multiplied with M_d^{-1} to determine turbulence inputs $\vec{u}_d$ for a decoupled system. Using $\vec{u}_d$ as second input, the output $\vec{y}$ is calculated

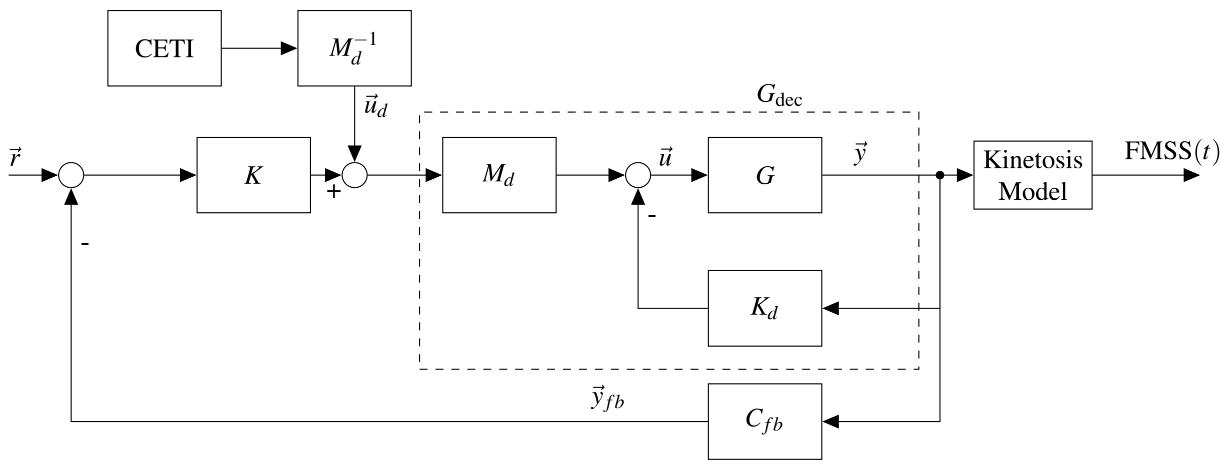

Figure 5: Analyzed ACAH control architecture.

according to Eq. (11)

$$\vec{y} = T(s)\cdot\vec{r} + S(s)\cdot G_{\text{dec}}(s)\cdot\vec{u}_d,$$
$$T(s) = G_{\text{dec}}\cdot(I+G_{\text{dec}})^{-1}, \quad S(s) = (I+G_{\text{dec}})^{-1}. \tag{11}$$

CONTROLLER MODIFICATION TO NEW DRBS

Since G_{dec} is calculated using decoupling procedure of Falb and Wolowich (Ref. 12), the system in Figure 5 can be simplified to four SISO systems. The output $\vec{y}$ of the system G_{dec} is also the input to the linearized kinetosis model. Multipling the output $\vec{y}$ of Eq. (11) with the respective entries of the linearized model G_{MS} from Eq. (16) leads to the relation of the motion sickness depending on the disturbances as shown in Eq. (12)

$$\Delta\vec{v} = G_{\text{MS}}\cdot(T(s)\cdot\vec{r} + S(s)\cdot G_{\text{dec}}(s)\cdot\vec{u}_d). \tag{12}$$

Since the input $\vec{r}$ should not consist of vibrations that increase the motion sickness $\Delta\vec{v}$, only the disturbance input $\vec{u}_d$ is considered. Therefore, the term $G_{\text{MS}}\cdot S(s)\cdot G_{\text{dec}}(s)$ is to be minimized. Here, the sensitivity function is the factor that can most be effected by the controller design. The DRB is used as a parameter to describe the sensitivity function. Therefore, new DRBs are defined.

Definition of new DRBs

The new DRBs are determined as the frequency of the peak values of the conflict transfer functions ${}_{\Delta vy}G_{fa_\phi}$ and ${}_{\Delta vx}G_{fa_\theta}$. This guarantees that disturbances at the peak frequency will still be attenuated. The new DRBs are defined as $\omega_{\text{DRB},\phi} = 1.0$ rad/s and $\omega_{\text{DRB},\theta} = 1.58$ rad/s for the roll and pitch axis, respectively as shown in Table 1.

	$\omega_{\text{DRB},\phi}$ in rad/s	$\omega_{\text{DRB},\theta}$ in rad/s
ADS-33 (Ref. 2)	0.9	0.5
New DRBs	1.0	1.58

Table 1: Values of new DRBs.

The new DRBs are analyzed using the nonlinear model. Therefore several PID controllers with different bandwidths are designed in pitch and roll direction. These controllers, designed with a open-loop phas margin of 60°, are analyzed within the control architecture in Figure 5 under medium turbulences using the CETI model. Within the simulation framework, the rotorcraft is exposed to turbulences for 1200 seconds (20 minutes). The kinetosis is simulated using the nonlinear conflict model from Ref. 6.

In Figure 6, the resulting motion sickness after 20 minutes is shown for different bandwidths in pitch direction. At each

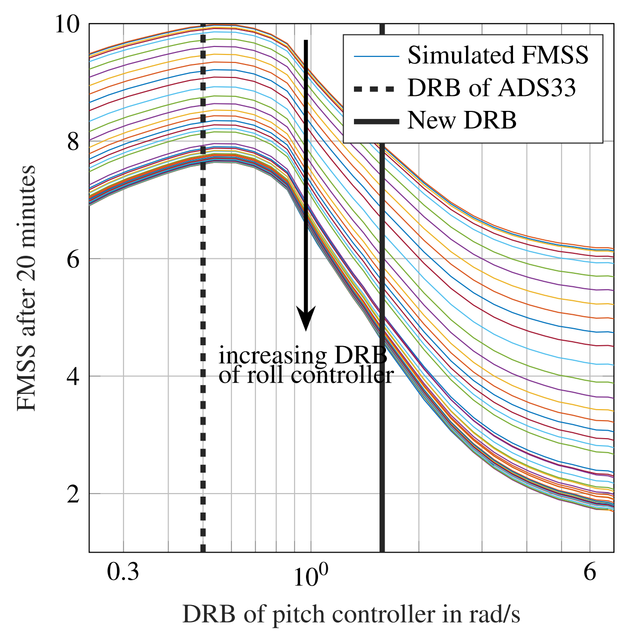

Figure 6: Resulting FMSS using controllers with different DRBs in pitch and roll direction.

curve, one controller in roll direction is used while in pitch direction controllers with increasing bandwidths er examined. It can be seen that the curves are all in the same shape and therefore, the change inducted with the pitch controller are independent from the roll controller. It can also be seen that the DRB of ADS-33 in this direction is at the peak of the discomfort while the new DRB shows a significant decrease.

To describe the detailed characteristics of the curve, in Figure 7 the change in FMSS over the DRB is shown. Therefore, the derivative in the logarithmic scale is calculated. It is confirmed that the DRB of ADS-33 close to the peak of the FMSS. It also can be seen that new DRB is over the turning point of the functions. Therefore, a further increasing of the bandwidth would only result in smaller improvement of ride comfort. The motion sickness after 20 minutes for different

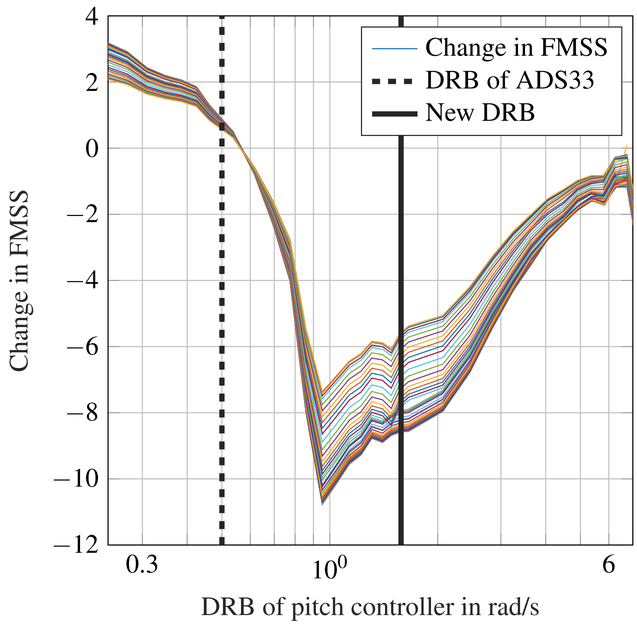

Figure 7: Change in FMSS for pitch controllers with different DRBs.

bandwidths in roll direction and the respective derivations are shown in Figure 12 and Figure 13 in the Appendix. For each curve, one controller in pitch direction is used whereas controllers with increasing bandwidth are examined in the roll direction.

Controller Adaption

The determined sensitivity functions for the closed-loop system with the initial controller are shown in Figure 8 and Figure 11. As stated above, the focus is limited within the paper to the roll and pitch axis since they contribute most to the subjective vertical conflict vector. As shown in Figure 8 and Figure 11, disturbances in the peak range of the kinetosis (purple lines) are amplified or transmitted undiminished to the attitude angles if the gains of the PI controller are set such that the DRBs from the ADS-33 are just maintained. Consequently, if controllers are designed that slightly fulfill the requirements of the DRBs, good handling qualities can be expected, but not good ride qualities.

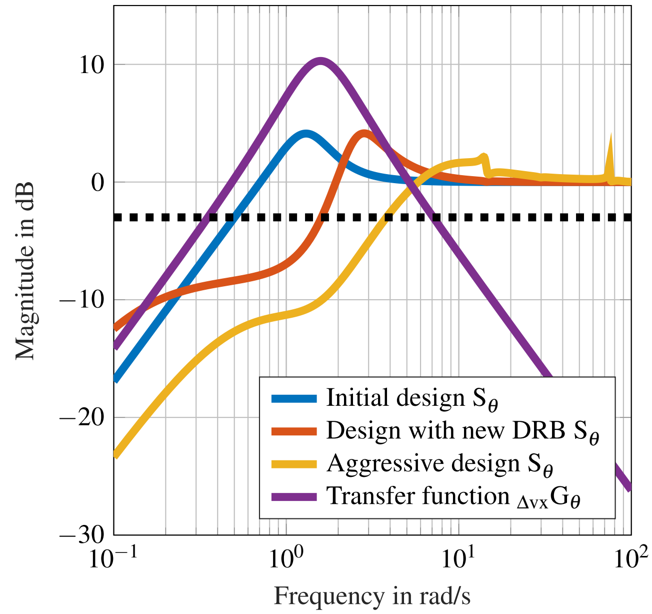

Figure 8: Closed-loop sensitivity function in pitch direction.

A new controller is developed tuning the gains of the PI controller to achieve the new bandwidths while maintaining the desired 60° phase margin of the open-loop system. The phase margin ensures that the peak of the sensitivity function does not exceed a certain value. The new controller design provides sensitivity functions (orange lines) that comply with the new DRBs, as seen from the intersection with the -3 dB line in Figure 8 and Figure 11.

In addition, a more aggressive controller (yellow lines) is designed. The structure of this controller is extended for a derivative control part. This allows to reach DRBs of $\omega_{\mathrm{DRB},\phi} = 3.28$ rad/s in roll direction and $\omega_{\mathrm{DRB},\theta} = 4.42$ rad/s in pitch direction while keeping the peak at a low level. As can be seen on Figure 8 and Figure 11, the aggressive controller provides jumps at frequencies of $\omega = 15$ rad/s and $\omega = 75$ rad/s. These are indications for poles and numerator zeros being close to each other. Therefore it is noted that the aggressive design is only used to demonstrate how low the kinetosis under the given flight conditions can be reduced and not to be used as a real controller design. Moreover, controllers with a higher bandwidth provide an unstable beahviour and result in controller inducted vibrations that increase the kinetosis.

SIMULATION RESULTS

To show the improvement through the adjustments, the initial controller is compared to the new controller and the aggressive controller regarding the sickness severity in a simulation framework. The resulting FMSS curves are shown in Figure 9 for all investigated controllers. At the end of the exposure time, the controller that complies with the old DRBs leads to FMSS $= 9.4$, while the controller that complies with the new DRBs yields FMSS $= 6.8$. This is 28% lower than the baseline. The DRB of the aggressive controller leads to FMSS $= 2.4$ which is 75% below the baseline. This is close to be the minimum that can be provided within the system us-

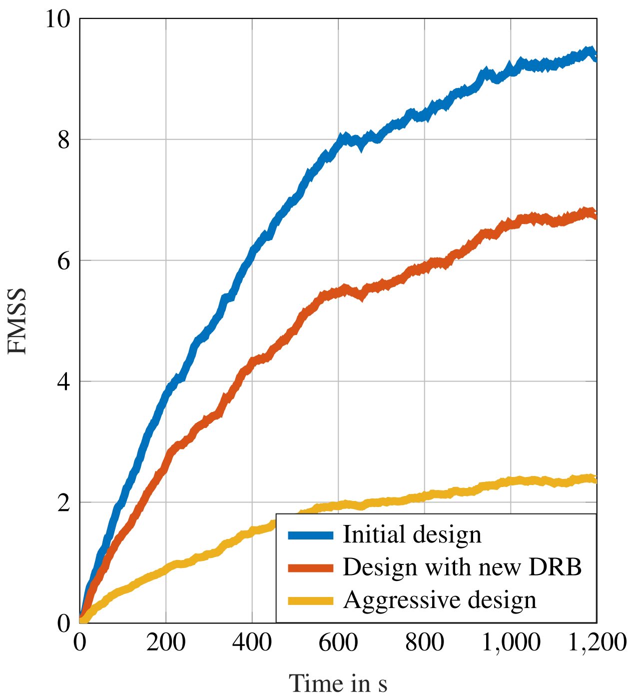

Figure 9: Simulated kinetosis severities.

ing PID controllers.
It can be seen that the rather small changes to the DRBs already lead to a significant reduction of the discomfort. With further increasing of the bandwidth, the improvement of ride comfort becomes smaller. Therefore, a controller designed with these new DRBs avoids the main frequencies that lead to kinetosis and therefore ensures better ride comfort.

CONCLUSIONS

Within the paper, an established model for the prediction of kinetosis was linearized. The characteristics of the linearized model in comparison to the original nonlinear model were identified leading to the following conclusions:

1. The ride comfort is significantly affected by the DRB of the sensitivity function. The DRBs given in the ADS-33 are not suitable to reduce motion sickness. New DRBs are required.
2. The new bandwidths are not contrary to the handling qualities requirements, so that a degradation of the handling qualities is not to be expected.
3. The linearization of the nonlinear kinetosis model is appropriate and accurate to derive new requirements for the disturbance rejection properties.

In summary, the new DRBs provide a stable controller and a significant reduction of kinetosis enabling a smooth and good ride during medium turbulences. Furthermore, the linearized kinetosis model allows the investigation on actively controlling the subjective vertical conflict which causes the symptoms of kinetosis.

Author contact:

Tim Burkhardt:	tim.burkhardt@ifr.uni-stuttgart.de
Süleyman Özkurt:	sueleyman.oezkurt@ifr.uni-stuttgart.de
Walter Fichter:	fichter@ifr.uni-stuttgart.de

APPENDIX A - PLOT RESULTS IN PITCH DIRECTION

In the paper, the Sensitivity functions and the results for simulations varying around one axis are only shown for the pitch direction. In the following, the plots for the roll direction are shown.

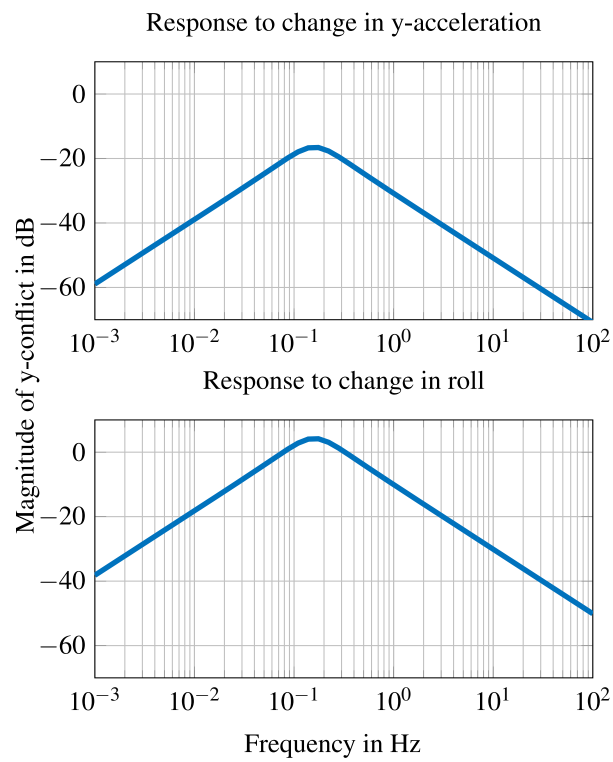

Figure 10: System response of the conflict to exemplary inputs.

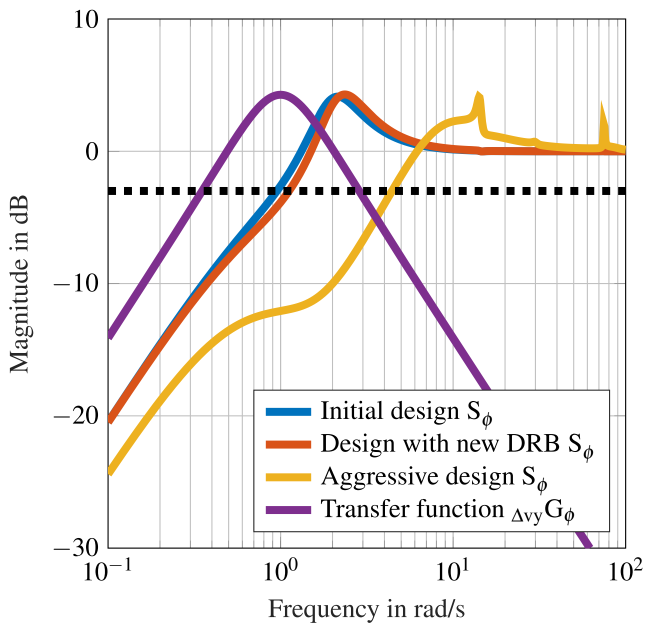

Figure 11: Closed-loop sensitivity function in roll direction.

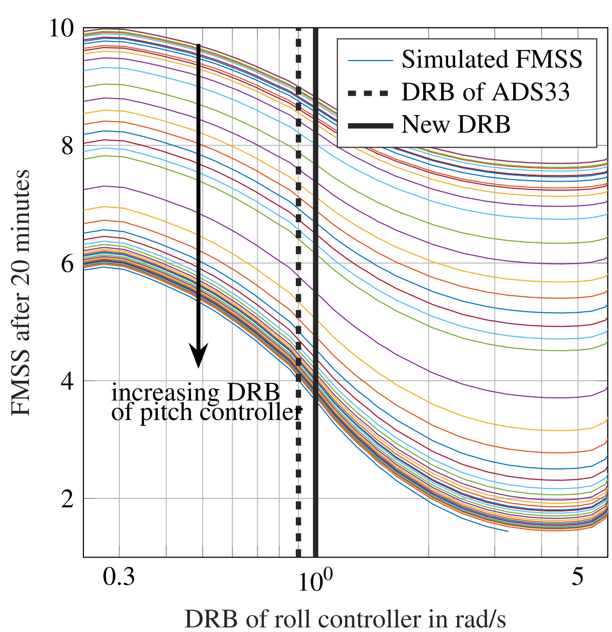

Figure 12: Resulting FMSS using controllers with different DRBs in roll and pitch direction.

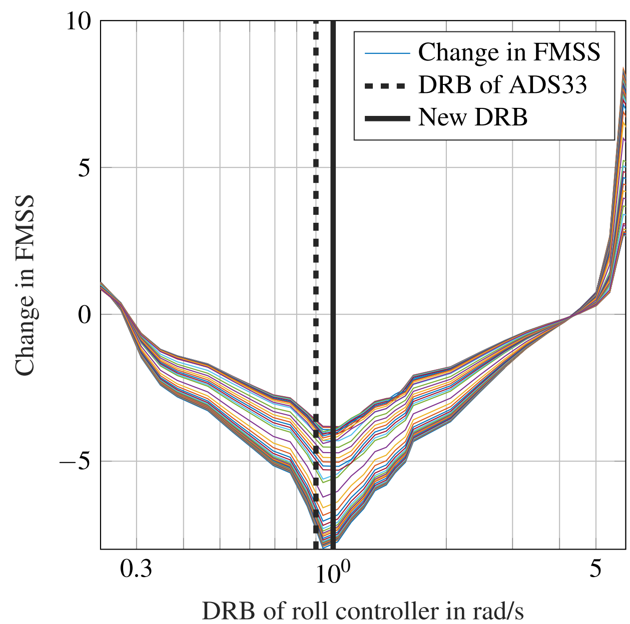

Figure 13: Change in FMSS for roll controllers with different DRBs.

APPENDIX B - LINEARIZATION OF THE KINETOSIS MODEL

$$
\begin{pmatrix} \dot{\vec{v}}_s \\ \dot{\hat{\vec{v}}}_s \\ \dot{\vec{\omega}}_{s2} \\ \ddot{\vec{\omega}}_{s2} \\ \dot{\hat{\vec{\omega}}}_{s1} \\ \Delta\dot{\vec{a}}_I \\ \Delta\dot{\vec{v}}_I \end{pmatrix} = \begin{bmatrix} \frac{\mathbf{1}}{\tau} \cdot ({}_k\vec{a} +_k \vec{g} - \vec{v}_s) - (-2 \cdot \dot{\vec{\omega}}_{s2} - \frac{1}{\tau_d \cdot \tau_a} \cdot \vec{\omega}_{s2} +_k \vec{\omega}) \times \vec{v}_s \\ \frac{\mathbf{1}}{\tau} \cdot (K_{ac} \cdot \Delta\vec{a}_I + K_{vc} \cdot \Delta\vec{v}_I + K_a \cdot_k \vec{a} - \hat{\vec{v}}_s) - (\frac{\tau_d \cdot K_{\omega c}}{\tau_d + \tau_d \cdot K_{\omega c}} \cdot (-2 \cdot \dot{\vec{\omega}}_{s2} - \frac{1}{\tau_d \cdot \tau_a} \cdot \vec{\omega}_{s2} +_k \vec{\omega}) - \frac{1}{\tau_d + \tau_d \cdot K_{\omega c}} \cdot \hat{\vec{\omega}}_{s1} + \frac{\tau_d \cdot K_\omega}{\tau_d + \tau_d \cdot K_{\omega c}} \cdot_k \vec{\omega}) \times \hat{\vec{v}}_s \\ 1 \cdot \dot{\vec{\omega}}_{s2} \\ -2 \cdot \dot{\vec{\omega}}_{s2} - \frac{1}{\tau_d \cdot \tau_a} \cdot \vec{\omega}_{s2} +_k \vec{\omega} \\ \frac{\tau_d \cdot K_{\omega c}}{\tau_d + \tau_d \cdot K_{\omega c}} \cdot (-2 \cdot \dot{\vec{\omega}}_{s2} - \frac{1}{\tau_d \cdot \tau_a} \cdot \vec{\omega}_{s2} +_k \vec{\omega}) - \frac{1}{\tau_d + \tau_d \cdot K_{\omega c}} \cdot \hat{\vec{\omega}}_{s1} + \frac{\tau_d \cdot K_\omega}{\tau_d + \tau_d \cdot K_{\omega c}} \cdot_k \vec{\omega} \\ -\vec{v}_s + \hat{\vec{v}}_s - K_{ac} \cdot \Delta\vec{a}_I - K_{vc} \cdot \Delta\vec{v}_I - K_a \cdot_k \vec{a} +_k \vec{a} +_k \vec{g} \\ \vec{v}_s - \hat{\vec{v}}_s \end{bmatrix} \tag{13}
$$

$$
A_{\mathrm{MS}}\vec{x}_{\mathrm{MS}} = \begin{bmatrix} -\frac{1}{\tau} & 0 & 0 & 0 & 0 & 0 & 0 \\ 0 & -\frac{1}{\tau} & 0 & 0 & 0 & \frac{1}{\tau}K_{ac} & \frac{1}{\tau}K_{vc} \\ 0 & 0 & 0 & 1 & 0 & 0 & 0 \\ 0 & 0 & -\frac{1}{\tau_d \cdot \tau_a} & -2 & 0 & 0 & 0 \\ 0 & 0 & -\frac{\tau_d \cdot K_{\omega c}}{\tau_d + \tau_d \cdot K_{\omega c}} \frac{1}{\tau_d \cdot \tau_a} & -2\frac{\tau_d \cdot K_{\omega c}}{\tau_d + \tau_d \cdot K_{\omega c}} & -\frac{1}{\tau_d + \tau_d \cdot K_{\omega c}} & 0 & 0 \\ -1 & 1 & 0 & 0 & 0 & -K_{ac} & -K_{vc} \\ 1 & -1 & 0 & 0 & 0 & 0 & 0 \end{bmatrix} \begin{bmatrix} \vec{v}_s \\ \hat{\vec{v}}_s \\ \vec{\omega}_{s2} \\ \dot{\vec{\omega}}_{s2} \\ \hat{\vec{\omega}}_{s1} \\ \Delta\vec{a}_I \\ \Delta\vec{v}_I \end{bmatrix} \tag{14}
$$

$$
B_{\mathrm{MS}}\vec{u}_{\mathrm{MS}} = \begin{bmatrix} \frac{1}{\tau_x} & 0 & 0 & 0 & -g\frac{1}{\tau_x} & 0 & 0 & 0 & 0 \\ 0 & -\frac{1}{\tau_y} & 0 & -g\frac{1}{\tau_y} & 0 & 0 & 0 & 0 & 0 \\ 0 & 0 & -\frac{1}{\tau_z} & 0 & 0 & 0 & 0 & 0 & 0 \\ \frac{1}{\tau_x}K_a & 0 & 0 & 0 & 0 & 0 & 0 & 0 & 0 \\ 0 & -\frac{1}{\tau_y}K_a & 0 & 0 & 0 & 0 & 0 & 0 & 0 \\ 0 & 0 & -\frac{1}{\tau_z}K_a & 0 & 0 & 0 & 0 & 0 & 0 \\ 0 & 0 & 0 & 0 & 0 & 0 & 0 & 0 & 0 \\ 0 & 0 & 0 & 0 & 0 & 0 & 0 & 0 & 0 \\ 0 & 0 & 0 & 0 & 0 & 0 & 0 & 0 & 0 \\ 0 & 0 & 0 & 0 & 0 & 0 & 1 & 0 & 0 \\ 0 & 0 & 0 & 0 & 0 & 0 & 0 & -1 & 0 \\ 0 & 0 & 0 & 0 & 0 & 0 & 0 & 0 & -1 \\ 0 & 0 & 0 & 0 & 0 & 0 & \frac{\tau_d \cdot K_{\omega c}}{\tau_d + \tau_d \cdot K_{\omega c}} + \frac{\tau_d \cdot K_\omega}{\tau_d + \tau_d \cdot K_{\omega c}} & 0 & 0 \\ 0 & 0 & 0 & 0 & 0 & 0 & 0 & -\frac{\tau_d \cdot K_{\omega c}}{\tau_d + \tau_d \cdot K_{\omega c}} - \frac{\tau_d \cdot K_\omega}{\tau_d + \tau_d \cdot K_{\omega c}} & 0 \\ 0 & 0 & 0 & 0 & 0 & 0 & 0 & 0 & -\frac{\tau_d \cdot K_{\omega c}}{\tau_d + \tau_d \cdot K_{\omega c}} - \frac{\tau_d \cdot K_\omega}{\tau_d + \tau_d \cdot K_{\omega c}} \\ -K_a + 1 & 0 & 0 & 0 & -g & 0 & 0 & 0 & 0 \\ 0 & K_a - 1 & 0 & -g & 0 & 0 & 0 & 0 & 0 \\ 0 & 0 & K_a - 1 & 0 & 0 & 0 & 0 & 0 & 0 \\ 0 & 0 & 0 & 0 & 0 & 0 & 0 & 0 & 0 \\ 0 & 0 & 0 & 0 & 0 & 0 & 0 & 0 & 0 \\ 0 & 0 & 0 & 0 & 0 & 0 & 0 & 0 & 0 \end{bmatrix} \begin{bmatrix} {}_f a_x \\ {}_f a_y \\ {}_f a_z \\ \Delta\phi \\ \Delta\theta \\ \Delta\psi \\ {}_f \omega_x \\ {}_f \omega_y \\ {}_f \omega_z \end{bmatrix} \tag{15}
$$

$$
\begin{aligned}
G_{\mathrm{MS}} &= \begin{bmatrix} {}_{\Delta vx}G_{{}_f a_x} & {}_{\Delta vx}G_{{}_f a_y} & {}_{\Delta vx}G_{{}_f a_z} & {}_{\Delta vx}G_\phi & {}_{\Delta vx}G_\theta & {}_{\Delta vx}G_\psi & {}_{\Delta vx}G_p & {}_{\Delta vx}G_q & {}_{\Delta vx}G_r \\ {}_{\Delta vy}G_{{}_f a_x} & {}_{\Delta vy}G_{{}_f a_y} & {}_{\Delta vy}G_{{}_f a_z} & {}_{\Delta vy}G_\phi & {}_{\Delta vy}G_\theta & {}_{\Delta vy}G_\psi & {}_{\Delta vy}G_p & {}_{\Delta vy}G_q & {}_{\Delta vy}G_r \\ {}_{\Delta vz}G_{{}_f a_x} & {}_{\Delta vz}G_{{}_f a_y} & {}_{\Delta vz}G_{{}_f a_z} & {}_{\Delta vz}G_\phi & {}_{\Delta vz}G_\theta & {}_{\Delta vz}G_\psi & {}_{\Delta vz}G_p & {}_{\Delta vz}G_q & {}_{\Delta vz}G_r \end{bmatrix} \\
&= \begin{bmatrix} \frac{\frac{1}{\tau_x}(1-K_a)s}{s^2 + \frac{1}{\tau_x}s + K_{ac}s + \frac{K_{vc}}{\tau_x}} & 0 & 0 & 0 & \frac{-g\frac{1}{\tau_x}s}{s^2 + \frac{1}{\tau_x}s + K_{ac}s + \frac{K_{vc}}{\tau_x}} & 0 & 0 & 0 & 0 \\ 0 & -\frac{\frac{1}{\tau_y}(1-K_a)s}{s^2 + \frac{1}{\tau_y}s + K_{ac}s + \frac{K_{vc}}{\tau_y}} & 0 & \frac{-g\frac{1}{\tau_y}s}{s^2 + \frac{1}{\tau_y}s + K_{ac}s + \frac{K_{vc}}{\tau_y}} & 0 & 0 & 0 & 0 & 0 \\ 0 & 0 & -\frac{\frac{1}{\tau_z}(1-K_a)s}{s^2 + \frac{1}{\tau_z}s + K_{ac}s + \frac{K_{vc}}{\tau_z}} & 0 & 0 & 0 & 0 & 0 & 0 \end{bmatrix}
\end{aligned} \tag{16}
$$

ACKNOWLEDGMENTS

This work is supported by the German Federal Ministry for Economic Affairs and Climate Action through the German Aviation Research Program LuFo VI-2 in the project AMI-HORATIO.

Supported by:

Federal Ministry
for Economic Affairs
and Energy

on the basis of a decision
by the German Bundestag

REFERENCES

1. Tischler, M. B., Ivler, C. M., and Mansur, M. H., "Handling-Qualities Optimization and Trade-offs in Rotorcraft Flight Control Design," Proceedings of the Royal Aeronautical Society of Rotorcraft Handling-Qualities Conference, November 2008.

2. ANON, "ADS-33E-PRF: Handling Qualities Requirements for Military Rotorcraft," , 2000.

3. ANON, "MIL-DTL-9490E: Flight Control Systems-Design, Installation and Test of Piloted Aircraft, General Specification For," , 2008.

4. Griffin, M. J., *Handbook of Human Vibration*, Academic Press, Southampton, U.K., 1990.

5. Özkurt, S., Fichter, W., Bülthoff, H., and Fischer, C., "On the Impact of Flight Control Systems on Kinetosis of Helicopter Passengers," 78th Annual Forum & Technology Display of the Vertical Flight Society, 05 2022. DOI: 10.4050/F-0078-2022-17522.

6. Özkurt, S., Burkhardt, T., Schimpf, F., and Fichter, W., "The Impact of Control Augmentation and Stability Augmentation System Parameters on Kinetosis of Rotorcraft Passengers," 79th Annual Forum & Technology Display of the Vertical Flight Society, 05 2023. DOI: 10.4050/F-0079-2023-18076.

7. ISO2631-1, *Mechanical vibration and shock - Evaluation of human exposure to whole-body vibration*, International Organization for Standardization, Genve, Switzerland, 1997.

8. Bos, J., and Bles, W., "Modelling motion sickness and subjective vertical mismatch detailed for vertical motions," *Brain research bulletin*, Vol. 47, 12 1998, pp. 537–42. DOI: 10.1016/S0361-9230(98)00088-4.

9. Mayne, R., *A Systems Concept of the Vestibular Organs*, Springer Berlin Heidelberg, Berlin, Heidelberg, 1974, pp. 493–580. DOI: 10.1007/978-3-642-65920-1_14.

10. Kamiji, N., Kurata, Y., Wada, T., and Doi, S., "Modeling and validation of carsickness mechanism," , 10 2007. DOI: 10.1109/SICE.2007.4421156.

11. Haslwanter, T., Jaeger, R., Mayr, S., and Fetter, M., "Three Dimensional Eye Movement Responses to Off-Vertical Axis Rotations in human," , 2000, pp. 96–106.

12. Falb, P. L., and Wolowich, W. A., "Decoupling in the Design and Synthesis of Multivariable Control Systems," *IEEE Transaction on Automatic Control*, Vol. AC-12, (6), December 1967, pp. 651–659.

13. Gahinet, P., Chen, R., and Eryilmaz, B., "Automated PID Controller Design," , June 2013.

14. Wang, Q.-G., Fung, H.-W., and Zhang, Y., "PID tuning with exact gain and phase margins," *ISA Transactions*, Vol. 38, (3), 1999, pp. 243–249.

15. Seher-Weiß, S., and von Grünhagen, W., "Development of EC135 Turbulence Models via System Identification," Proceedings of the 35th European Rotorcraft Forum, September 2009.